FLEXURE EXAMPLES

Primary reference:
Watts, A. B., *Isostasy and Flexure of the Lithosphere*, Cambridge University Press, 2001.

These notes provide practical examples of flexural models applied to structures in the oceanic and continental lithosphere. The models are all basically solutions to the thin-plate flexure equation with a variety of surface loads, sub surface loads, and boundary conditions. Both gravity and topography data are used to constrain the models. We'll see in a following lecture that gravity data provide important constraints on the topography of the moho. Figures and captions are provided on the following pages. In addition, a reference is provided for each figure. The features include:

- Seamount - undersea volcano loading the oceanic lithosphere;
- Trench – plate bending at a subduction zones;
- Fracture zone – flexure that accumulates due to the differential subsidence across an oceanic fracture zone;
- Normal fault – asymmetric topography due to normal faults mainly in continental crust;
- Thrust fault – asymmetric topography due to a thrust fault in the foreland basin adjacent to continental mountains;
- Rift – symmetrical but aborted continental rift which usually fills with sediment to form a *steer head* basin;
- Passive margin – symmetrical rift that evolves into a young ocean basin and accumulates continental sediments to become a passive continental margin; and
- Venus trench – flexural topography on Venus that is caused by thrust faulting and possibly earth-like subduction.

Seamount Data

4.3 Seamounts and Oceanic Islands 137

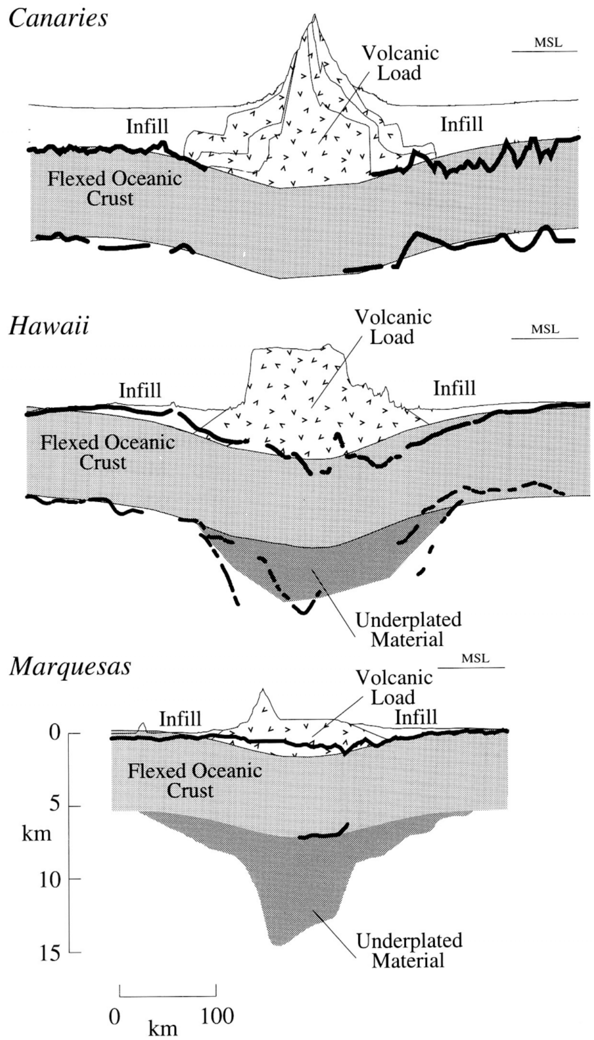

Fig. 4.21. Comparison of the crustal structure at the Canary (Watts et al., 1997), Hawaiian (Watts and ten Brink, 1989) and Marquesas (Caress et al., 1995) islands with the predictions of simple elastic plate models. Reproduced from Fig. 7 of Watts et al. (1997).

Watts, A. B., C. Pierce, C., J. Collier, R. Dalwood, J. Cannales, and T. J. Henstock, A seismic study of lithospheric flexure in the vicinity of Tenerife, Canary Islands, *Earth Planet Sci. Lett., 146*, p. 431-447, 1997.

Seamount Model

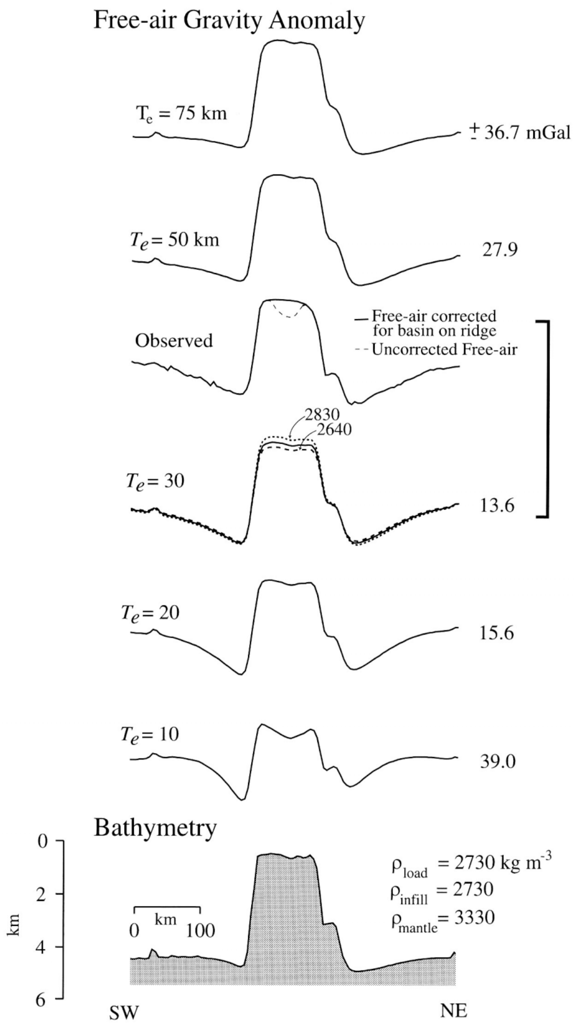

Fig. 4.16. Comparison of observed and calculated gravity anomalies along a profile that intersects the Hawaiian Islands between Oahu and Molokai. The observed profile is based on data acquired during cruise KK8213 of *R/V Kana Keoki*. The calculated profiles are based on an elastic plate model with T_e = 10, 20, 30, 50 and 75 km. The numbers on the right-hand side are the root mean square differences between observed and calculated anomalies.

Seamount Flexure vs. Age

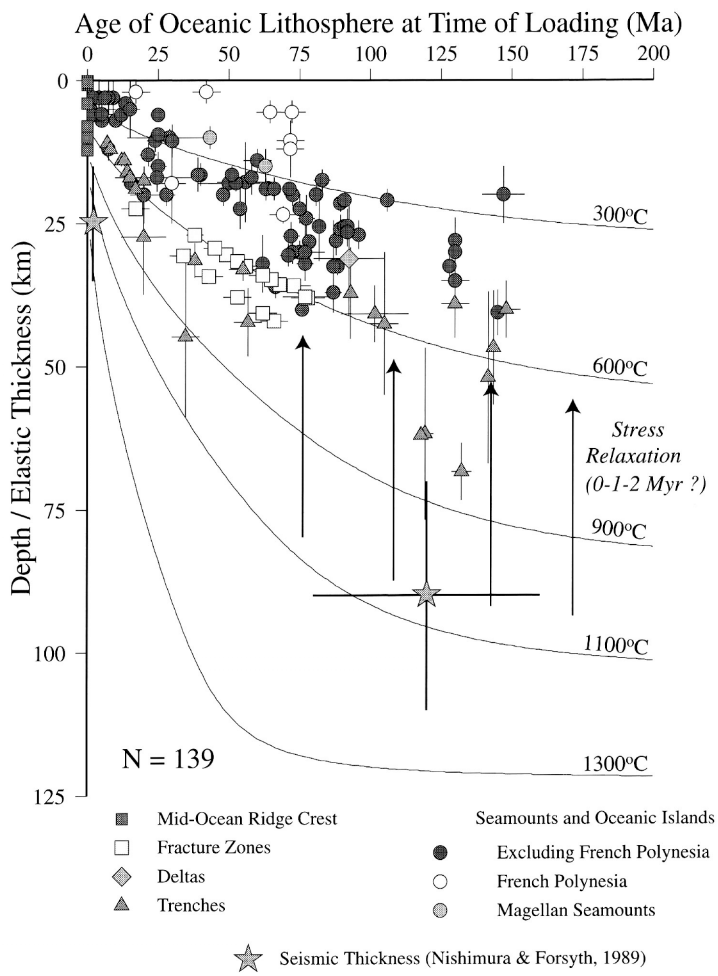

Fig. 6.11. Plot of T_e against $t_{sf} - t$, the age of the lithosphere at the time of loading. The colour coding is according to the type of geological feature.

Trench Model

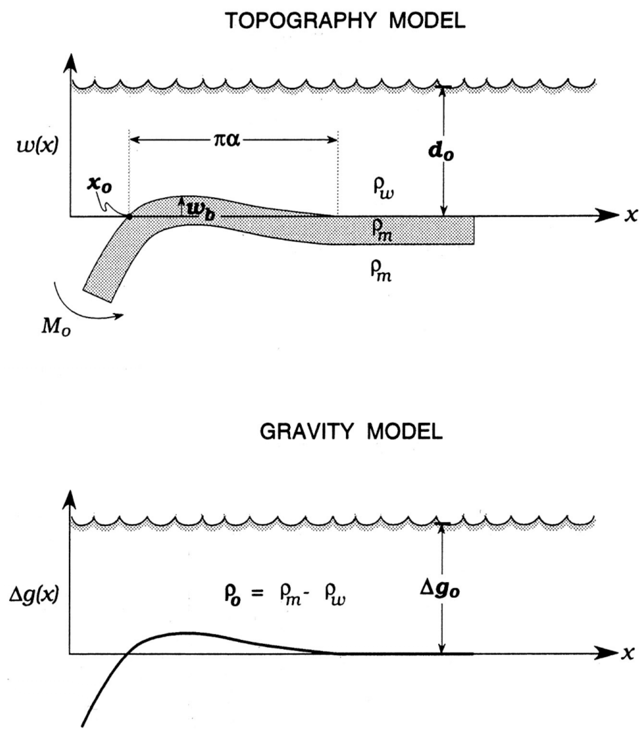

Figure 2. Schematic representation of topography (w_o, x_o, α, and d_o) and gravity (w_o, x_o, α, and g_o) model parameters, where $w_o \sim 3.10\, w_b$. See equations (3) and (5) for details of the model. Combined model (topograv) contains all of the above parameters and ρ_o. After application of a depth versus age correction, a regional slope parameter was not required. Topograv parameters are bold.

Levitt, D. A. and D. T. Sandwell, Lithospheric bending at subduction zones based on depth soundings and satellite gravity, *J. Geophys. Res.*, *100*, 379-400, 1995.

Trench Data

LEVITT AND SANDWELL: LITHOSPHERIC BENDING AT TRENCHES

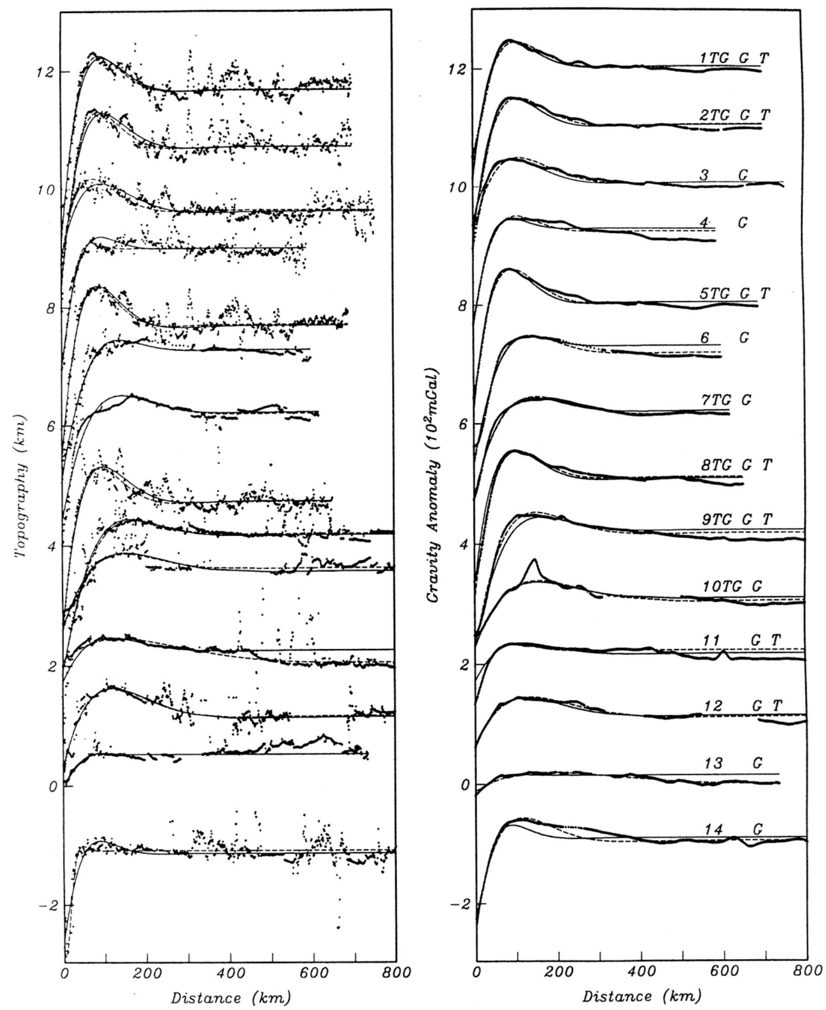

Figure 5. Topography and gravity data for 117 profiles modeled in the study. Profiles are arbitrarily shifted vertically for presentation. For topography (shown at left), solid lines correspond to the best fit model for topograv (λ = 0.4) and dashed lines correspond to the best fit model for topo (λ = 0). For gravity (shown at right), solid lines correspond to the best fit model for topograv (λ = 0.4) and dashed lines correspond to the best fit model for grav ($\lambda = \infty$). Profiles are numbered according to the numbering scheme of Table 1. TG, G, and T mark profiles that were "successfully" modeled by topograv, grav, and topo, respectively.

Levitt, D. A. and D. T. Sandwell, Lithospheric bending at subduction zones based on depth soundings and satellite gravity, *J. Geophys. Res.*, *100*, 379-400, 1995.

Outer Rise Normal Faults

Southern Tonga Trench [Massell, 2002]

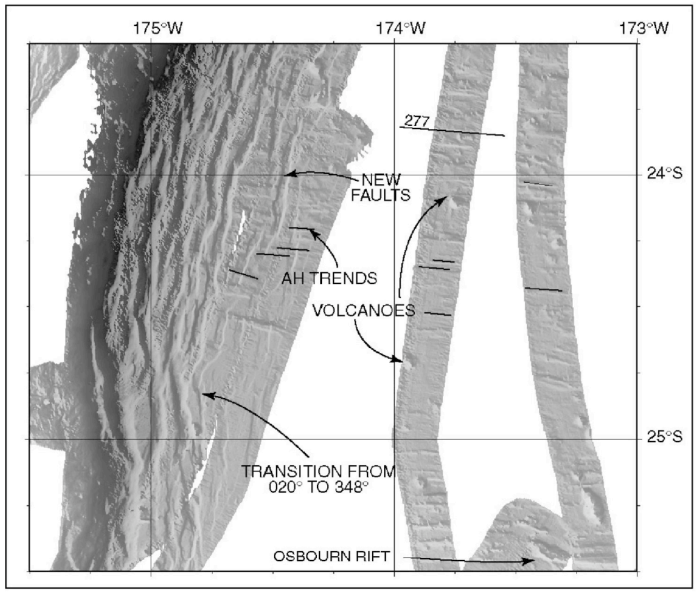

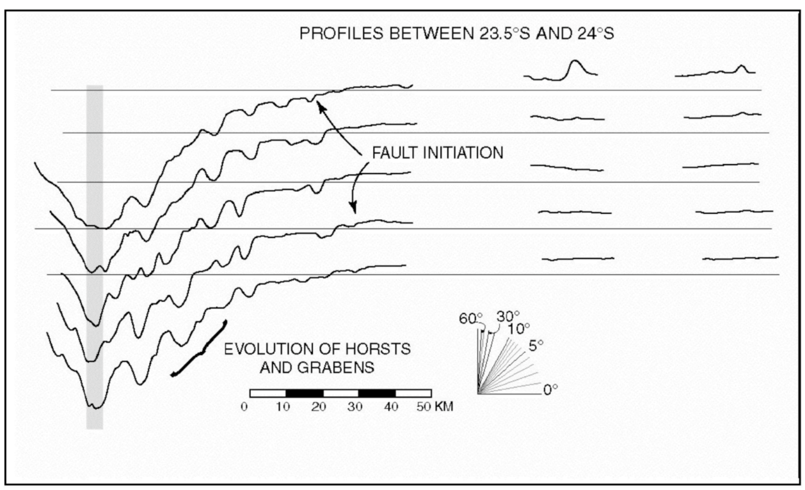

Massell, C., *Large Scale Structural Variation of Trench Outer Slopes and Rises*, Ph. D. Dissertation, Scripps Inst. of Oceanography, La Jolla, CA, 2002.

Brittle and Ductile Deformation

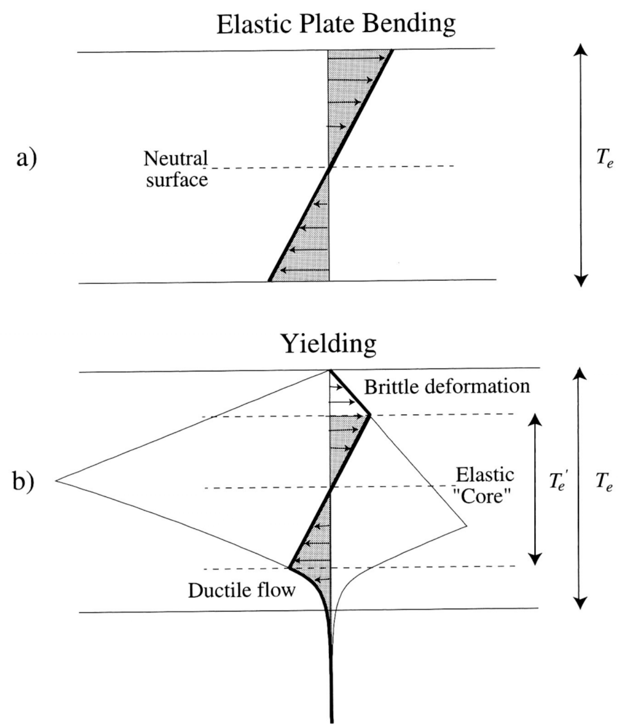

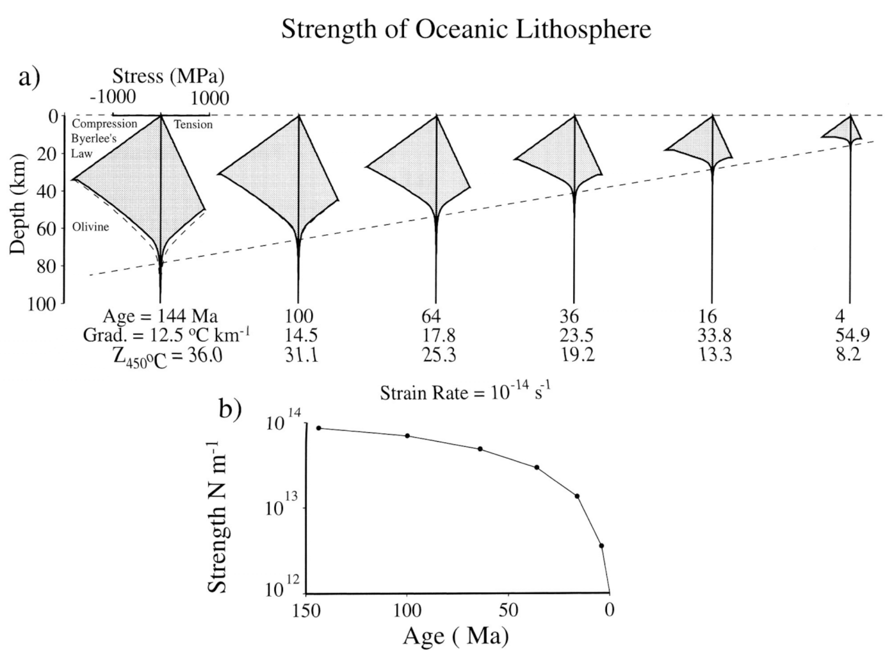

Fig. 6.27. Yield Strength Envelope and strength profiles for the oceanic lithosphere. (a) YSE for the cooling plate (solid lines) and half-space (dashed lines) models and for ages of lithosphere in the range 4–144 Ma. (b) Integrated strength of the lithosphere obtained by calculating the area under YSE at each time interval. Parameters defining the flow laws of olivine are as given in Table 6.4.

Trench Flexure and Earthquakes

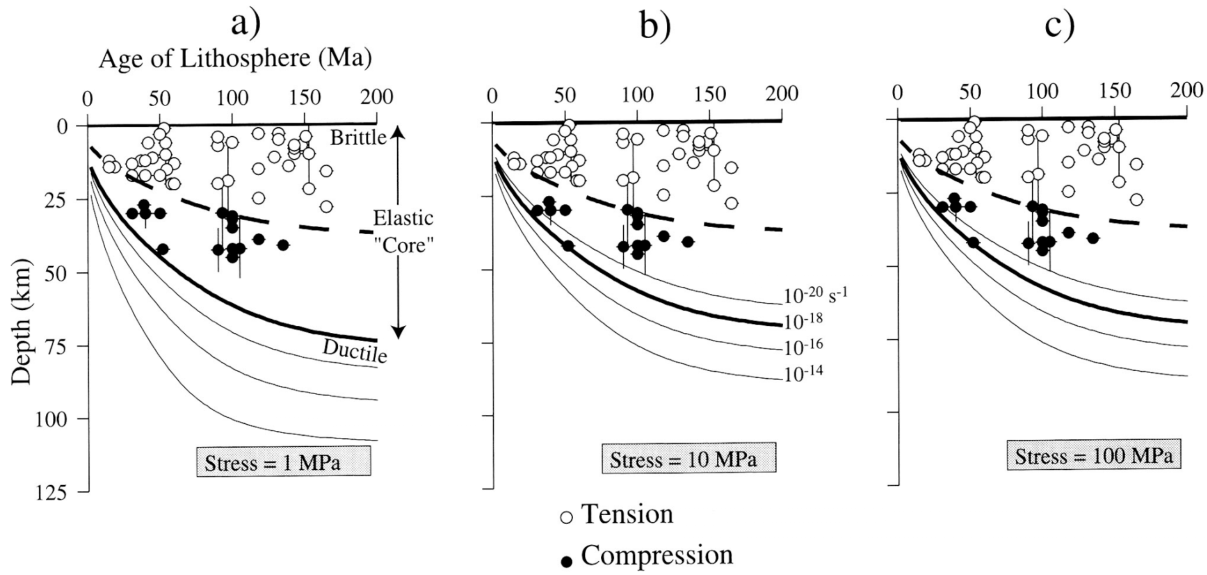

Fig. 6.37. Comparison of the depth and focal mechanisms of earthquakes in deep-sea trench–outer rise systems with the predictions of the Yield Strength Envelope (YSE) model. The earthquake data are based on a compilation by Seno and Yamanaka (1996). The YSE model is based on a thermal structure determined by the cooling plate model, an olivine rheology and the range of strain rates and applied stresses shown.

Seno, T. and Y. Yamanaka, Double seismic zones, compressional deep trench-outer rise events, and superplumes, in Bebout, G. E., D. Scholl, S. Kirby, and J. Platt, eds., *Subduction Top to Bottom, Monograph, 36*, Washington, DC, American Geophysical Union, pp. 347-355, 1996.

Trench Flexure and Saturation Bending Moment

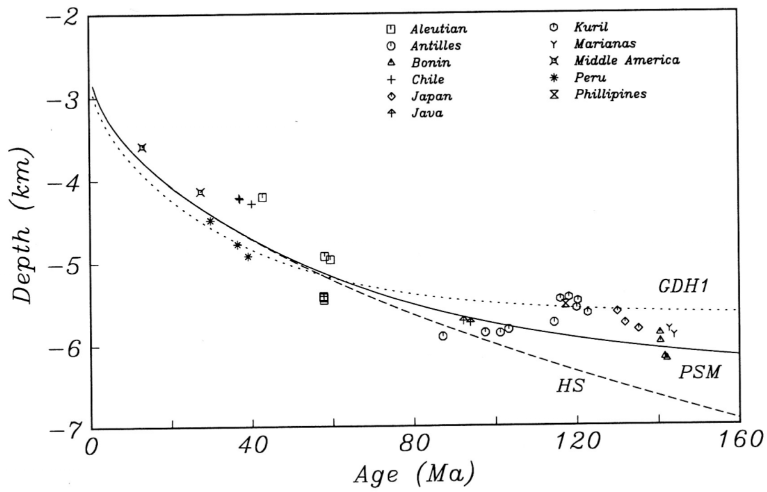

Figure 7. Best fit model depths at the first zero crossing with respect to model ages at the first zero crossing from a two-dimensional interpolation of an age grid [*Roest et al.*, 1992], with predicted depths according to the HS (dashed), PSM (solid), and GDH1 (dotted) thermal models. See key on figure for trench symbols.

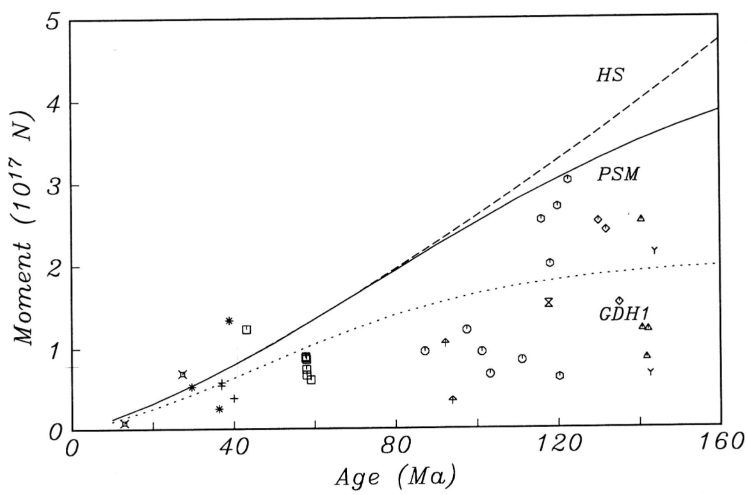

Figure 8. Bending moment values determined using the thin elastic plate model (equation (12)) with respect to model ages at the first zero crossing from a two-dimensional interpolation of an age grid [*Roest et al.*, 1992], with saturation moments predicted according to the HS (dashed), PSM (solid), and GDH1 (dotted) thermal models. Trench symbol assignment is identical to Figure 7.

Levitt, D. A. and D. T. Sandwell, Lithospheric bending at subduction zones based on depth soundings and satellite gravity, *J. Geophys. Res.*, *100*, 379-400, 1995.

Continental Yield Strength and Earthquakes

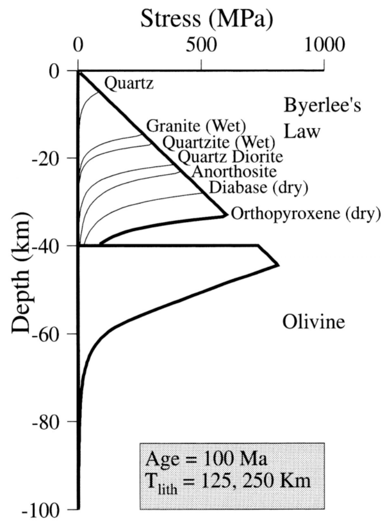

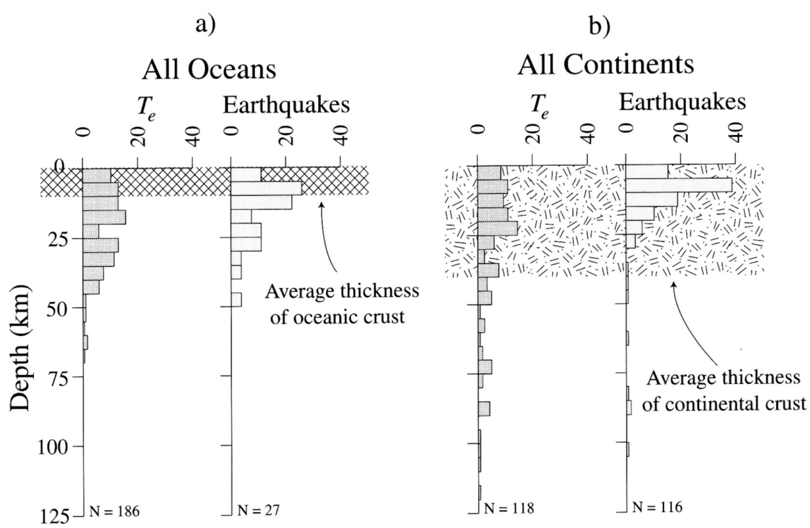

Fig. 6.40. Comparison of T_e with the depth of earthquakes in (a) oceans and (b) continents. The T_e data are based on data in Tables 6.1 and 6.2. The earthquake data are based on the compilations of Chen and Molnar (1983) and Wiens and Stein (1984).

Chen, C. P., and P. Molnar, Focal depths of intracontinental and intraplate earthquakes and their implications for the thermal and mechanical properties of the lithosphere, *J. Geophys. Res., 88*, pp. 4183-4214, 1983.

Weins, D.A. and S. Stein, Intraplate seismicity and stresses in young oceanic lithosphere, *J. Geophys. Res., 89*, pp. 11442-11464, 1984.

Fracture Zone Model

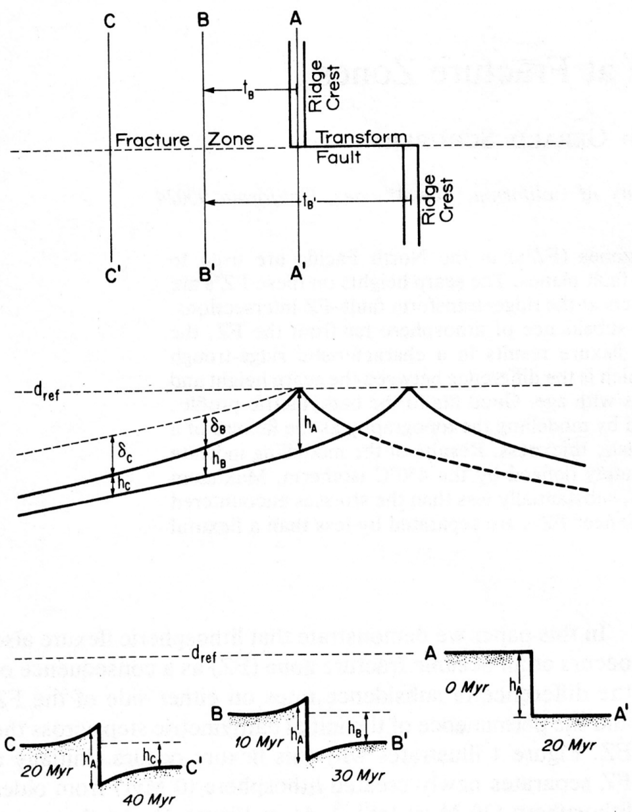

Fig. 1. Evolution of a fracture zone. (Top) Spreading ridges offset by a transform fault. The age offset across the FZ is $t_{B'} - t_B$. (Center) The h's are the differences in ocean floor depth between locations far to either side of the FZ. The initial height of the scarp at the FZ is h_A. If the FZ does not slip, the scarp height must remain constant. The constancy of scarp height and the decrease in h with age cause the lithosphere in the vicinity of the FZ to bend. The flexural amplitude δ_B is the difference between h_A and h_B. Similarly, $\delta_c = h_A - h_C$. (Bottom) Sketch of bathymetry along profiles A-A', B-B', and C-C' illustrating the lithospheric flexure described above.

Sandwell, D. T., and G. Schubert, Lithospheric Flexure at Fracture Zones, *J. Geophys. Res., 87*, 4657-4667, 1982.

Fracture Zone Data

Sandwell and Schubert: Lithosphere Flexure at Fracture Zones

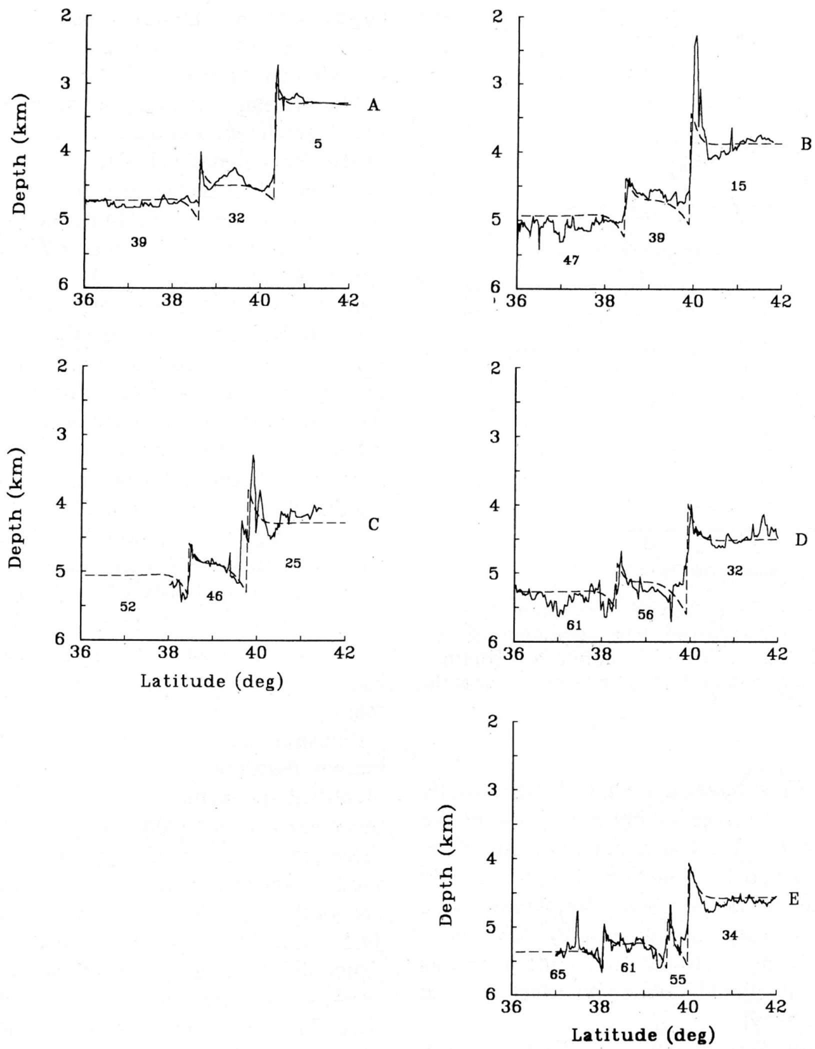

Fig. 6. Comparisons between theoretical bathymetric profiles computed from flexure models assuming no slip on the FZ's (dashed lines) and the observed bathymetric profiles A–E (solid lines). The asymmetric flexure predicted by the model across each FZ is a consequence of the increase in flexural wavelength with age according to (9). The apparent tilt in the bathymetry between the Pioneer and Mendocino FZ's occurs because the flexural wavelength is greater than their separation distance.

Sandwell, D. T., and G. Schubert, Lithospheric Flexure at Fracture Zones, *J. Geophys. Res., 87*, 4657-4667, 1982.

Normal Fault Model

Vening Meinesz hypothesis

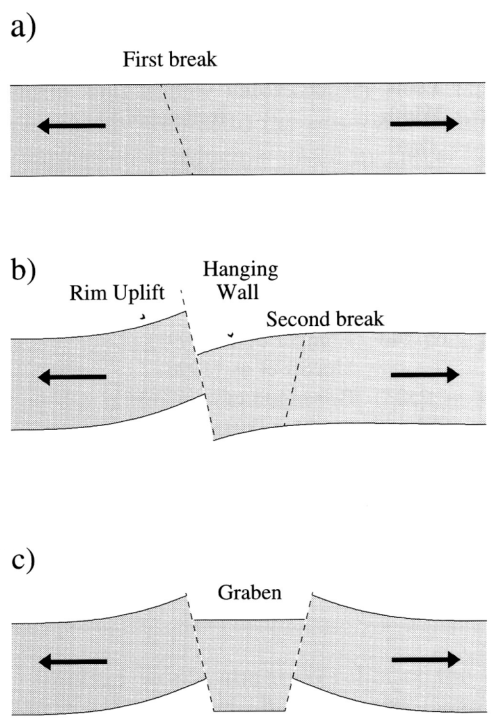

Fig. 7.4. Vening Meinesz's model for the development of a graben. Reproduced from Fig. 10D-1 of Heiskanen and Vening Meinesz (1958) with permission of McGraw-Hill Inc.

Normal Fault Data

296 *Isostasy and the Origin of Geological Features in the Continents and Oceans*

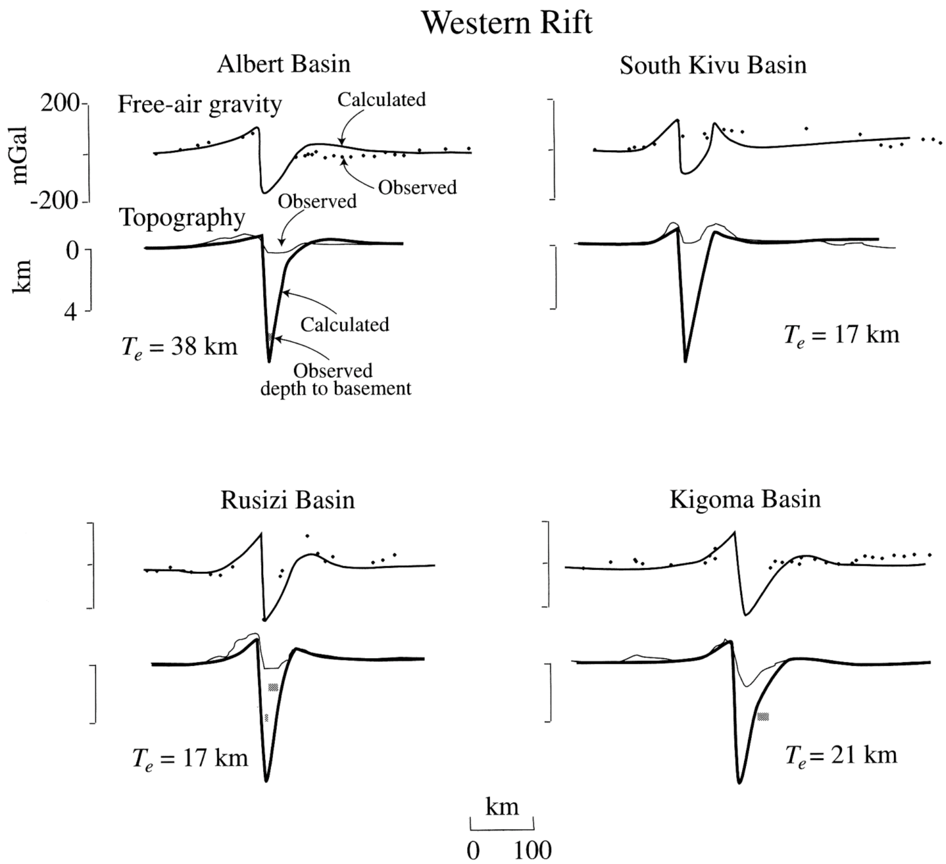

Fig. 7.8b. Comparison of the predictions of the Weissel and Karner (1989) model with free-air gravity anomaly, depth to basement and topography profile data over the Western Rifts of East Africa. Reproduced from Fig 11a–f of Ebinger et al. (1991), copyright by the American Geophysical Union.

Weissel, J. K., and G. D. Karner, Flexural uplift of rift flanks due to mechanical unloading of lithosphere during extension, *J. Geophys. Res., 94*, p. 13919-13950, 1989.

Ebinger, C. J., G. D. Karner, and J. K. Weissel, Mechanical strength of extended continental lithosphere: Constraints from the western rift system, Tectonics, 10, pp. 1239-1256, 1991.

Thrust Fault

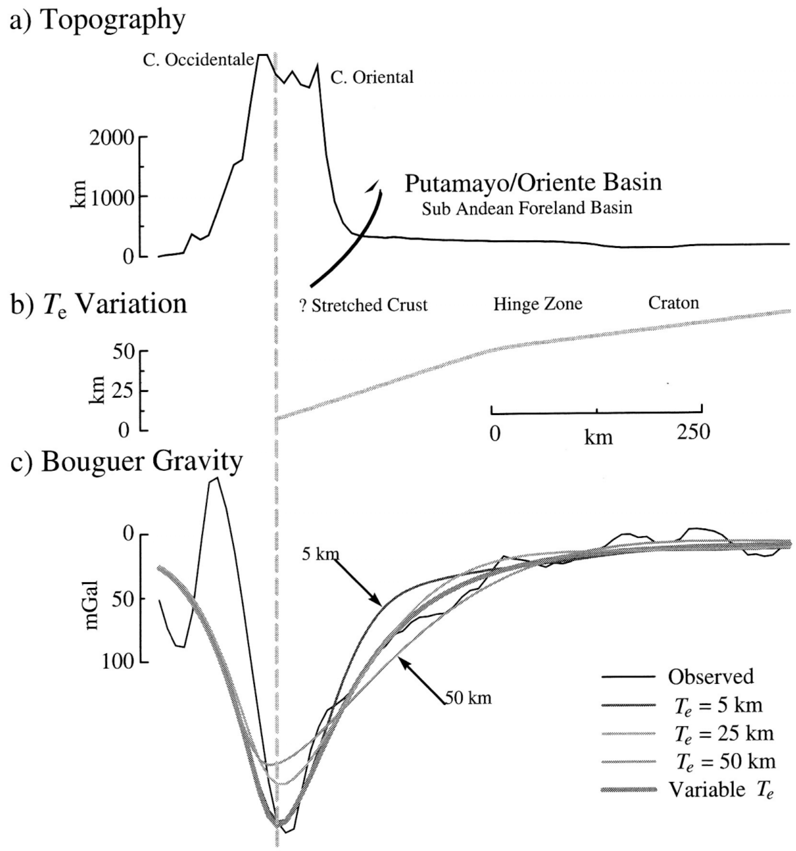

Fig. 7.50. Comparison of observed and calculated Bouguer gravity anomalies along a profile of the sub-Andean thrust and fold belt in Ecuador. The observed anomalies are based on a compilation by GETECH. The calculated anomalies are based on a broken plate model which is subject to a surface (topographic) load and an additional shear force of 0.50×10^{12} N m^{-1} that has been applied at the plate break. (a) Topography, (b) variation in T_e and (c) Bouguer gravity anomalies. Reproduced from Fig. 7 of Stewart and Watts (1997).

Stewart, J. and A. B. Watts, Gravity anomalies and spatial variations of flexural rigidity at mountain ranges, *J. Geophys. Res., 102*, pp. 5327-5352, 1997.

Continental Rift and Basin Evolution

332 *Isostasy and the Origin of Geological Features in the Continents and Oceans*

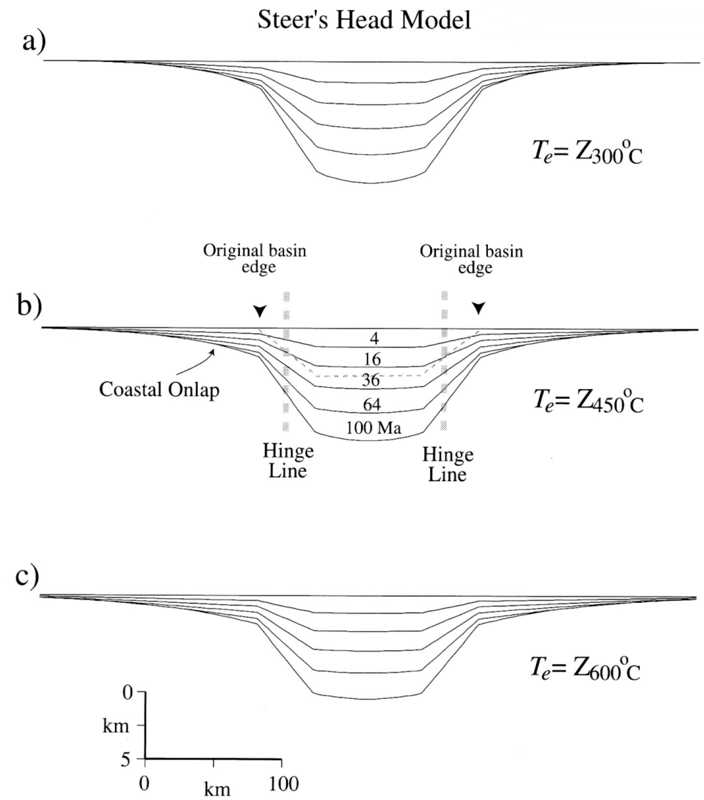

Fig. 7.28. The predicted stratigraphy of a basin, based on the tectonic subsidence model in Fig. 7.27. The stratigraphy has been computed by assuming that the sediments represents a load on the underlying lithosphere, which subsides under their weight. The calculations assume a T_e that increases with the age of loading, as defined by the depth to the (a) 300, (b) 450 and (c) 600°C isotherms. Each model is associated with "onlap"' of strata at their edges that is due to the increase in T_e with age. Modified from Fig. 4 of Watts et al. (1982).

Watts, A. B., G. D. Karner and M. S. Steckler, Lithospheric flexure and the evolution of sedimentary basins, *in The Evolution of Sedimentary Basins, V. 305a, Phil. Trans. R. Soc. Lond.,* pp 249-281, 1982.

Passive Margin Model

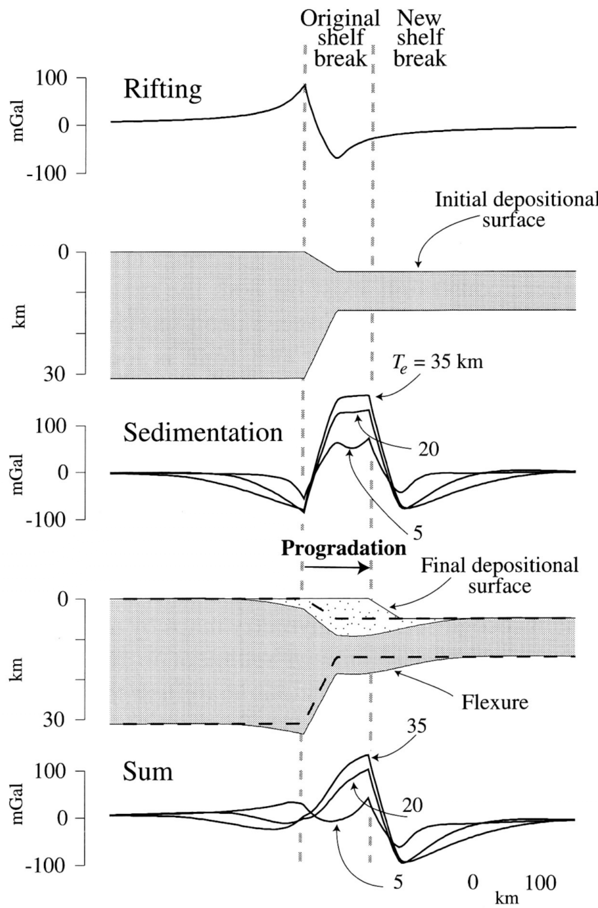

Fig. 4.39. Simple model showing the contributions to the gravity anomaly of a prograding sediment wedge. The net effect is to move the edge-effect anomaly associated with the initial margin seawards. The amplitude and wavelength of the calculated anomaly depends strongly on T_e with the largest amplitude anomalies being associated with the strong margin and smallest the weak margin.

Passive Margin Data

7.2 Extensional Tectonics and Rifting 327

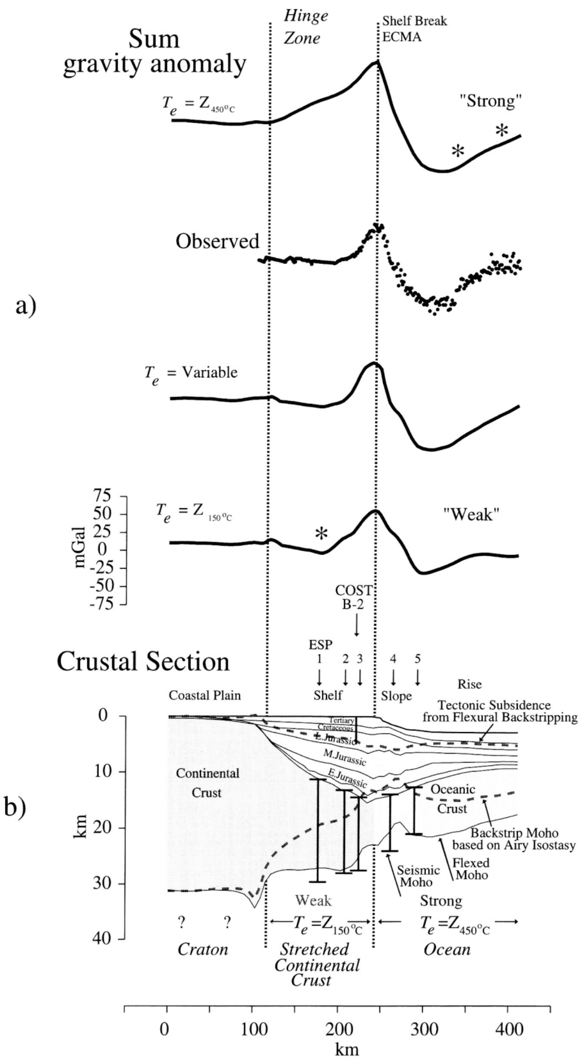

Fig. 7.25. The application of the "process oriented"' approach to seismic and gravity anomaly data at the East Coast, U.S. rifted margin. In this approach, sediments in a rift basin are progressively backstripped through time and the gravity anomalies due to the combined effects of rifting and sedimentation are computed for different assumed values of T_e. By comparing observed and calculated gravity anomalies it is possible to constrain T_e and, in some cases, its spatial and temporal variations. (a) observed (black dots) and calculated gravity anomalies. (b) crustal structure deduced from backstripping and gravity modelling. Reproduced from Figs. 6 and 7 of Watts and Marr (1995).

For a colour version of this figure, see the plate section.

Watts, A. B. and C. Marr, Gravity anomalies and the thermal and mechanical structure of rifted continental margins, *in Rifted Ocean-Continent Boundaries*, Kluwer Academic Publishers, Dordrecht, pp. 65-94, 1995.

Venus Trench Area

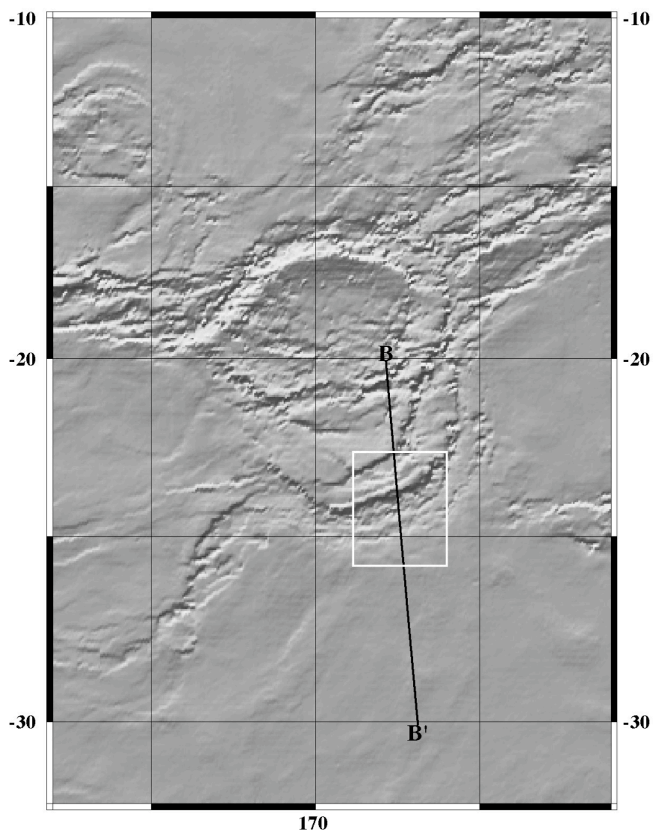

Sandwell, D. T. and G. Schubert, Evidence for Retrograde Lithospheric Subduction on Venus, *Science, 257,* 766-770, 1992.

Venus Trench Model

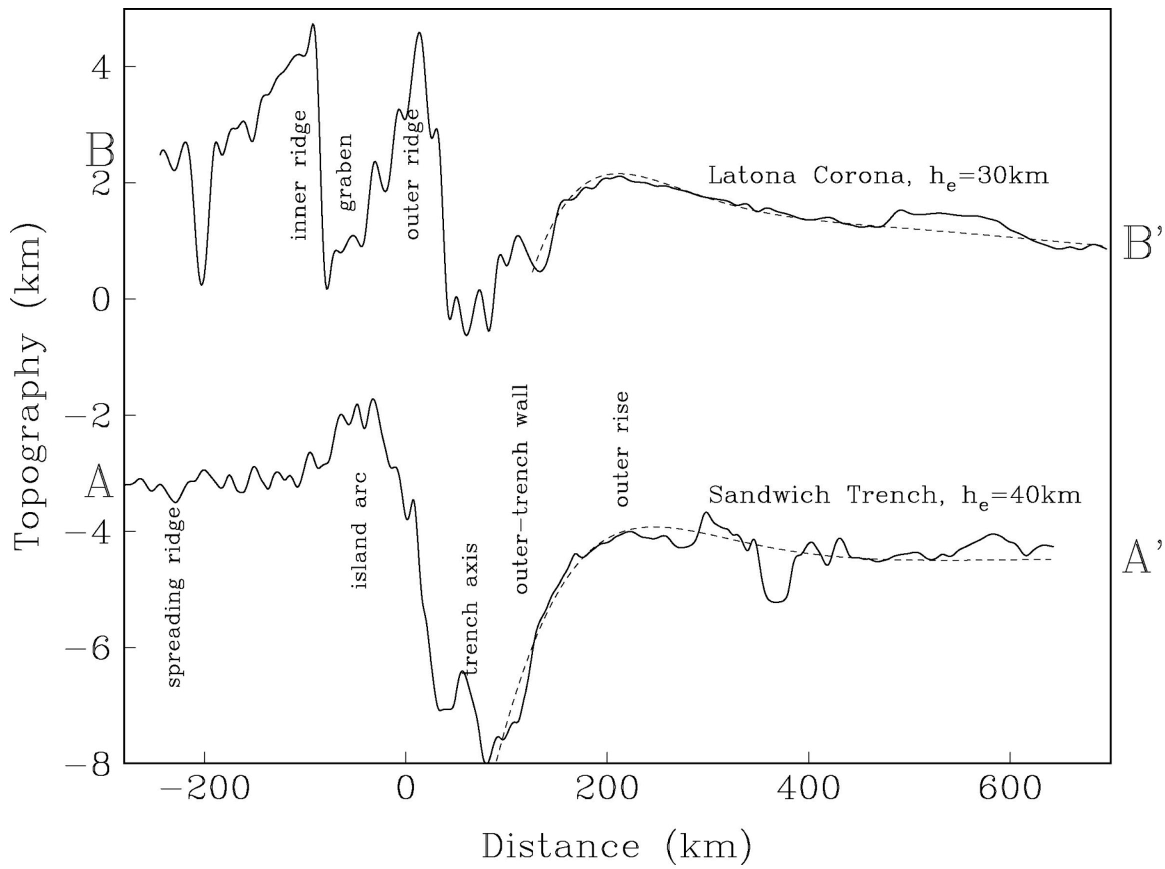

Sandwell, D. T. and G. Schubert, Evidence for Retrograde Lithospheric Subduction on Venus, *Science, 257,* 766-770, 1992.